Calculation Methods and Effects of End-Winding Inductance and Permanent-Magnet End Flux on Performance Prediction of Nonoverlap Winding Permanent-Magnet Machines

Johannes H. J. Potgieter, *Student Member, IEEE*, and Maarten J. Kamper, *Senior Member, IEEE*

***Abstract*—Due to the short end windings of nonoverlap winding permanent-magnet (PM) machines, the end-winding inductance component is generally ignored in the design. In most cases, the end-flux fringing effects in PMs are also not taken into account. It is shown in this paper that these end effects have a significant influence on the performance parameters of the machine. In this paper, several nonoverlap winding PM machines are considered with respect to the effects of end-winding inductance and PM end-flux fringing. A number of calculation methods for the per-phase end-winding inductance of the machines are compared. A new simple analytical calculation method is proposed, which is shown to give a relatively good prediction of the end-winding inductance compared with 3-D finite-element (FE) results. It is proposed in this paper that the PM strength should be reduced by a certain fringing factor to take the end-flux fringing effects into account in the 2-D FE analysis. Practical measurements are also presented to validate the FE calculations and to give an indication on the effects that are caused by the end-winding inductance and the PM end-flux fringing.**

***Index Terms*—Analytical models, design optimization, end windings, finite-element (FE) methods, flux fringing, inductance, permanent-magnet (PM) machines, saturation magnetization.**

Nomenclature

a, b, c	Dimensional parameters used in the calculation of $L_{e(1,2,3)}$ [mm].
B_r	Permanent-magnet (PM) remanence or residual inductance [T].
$D_{\rm ag}$	Air-gap diameter [mm].
$f_{1,2,3,4}$	Subfunctions used in the calculation of k_2.
h_c	Coil height [mm].
H_c	PM coercivity [kA/m].
h_g	Air-gap height [mm].
h_m	PM height [mm].
I_s	Rated current [A].
K, k_1, k_2	End-winding inductance calculation constants, with $K = k_1 - k_2$.
K_f	PM end-fringing factor.
K_M	End-winding mutual per-phase cross-coupling factor.
K_p	External permeability factor.
l	Axial stack length [mm].
l_e	Average end-winding length [mm].
l_g	Distance of the end winding from the stack [mm].
$L_{(a,b)}$	Inductance notations used for calculations with the method of mirror images [H].
$L_{e(1,2,3)}$	End-winding inductance component [H].
L_s	Per-phase inductance [H].
M_c	Mutual phase end-winding cross coupling [%].
n_a	Number of parallel circuits.
N_c	Number of turns per coil.
n_s	Rotor speed [r/min].
P_g	Electrical output power [kW].
q	Number of coils per phase.
r_c	Average coil radius [mm].
T_b	Maximum breakdown torque [N · m].
T_g	Rated torque [N · m].
V_s	Rated voltage [V].
v_w	Wind speed [m/s].
w_c	Coil width [mm].
w_t	Average tooth width [mm].
x, y	Input parameters in the calculation of k_2.
β	Input parameter in the calculation of k_1.
λ_s	Per-phase flux linkage [Wb · t].
λ_e	End-winding flux linkage [Wb · t].
λ_m	PM flux linkage [Wb · t].
σ_m	Magnet pitch to pole pitch ratio.

Manuscript received August 21, 2013; revised November 6, 2013; accepted December 9, 2013. Date of publication December 20, 2013; date of current version July 15, 2014. Paper 2013-EMC-616.R1, presented at the 2012 International Conference on Electrical Machines, Marseille, France, September 2–5, and approved for publication in the IEEE TRANSACTIONS ON INDUSTRY APPLICATIONS by the Electric Machines Committee of the IEEE Industry Applications Society. This work was supported in part by the National Research Foundation of South Africa.

J. H. J. Potgieter was with the Department of Electrical and Electronic Engineering, Faculty of Engineering, University of Stellenbosch, Stellenbosch 7600, South Africa. He is now with the Department of Engineering Science, University of Oxford, Oxford, OX1 3PJ, U.K. (e-mail: johannes.potgieter@eng.ox.ac.uk).

M. J. Kamper is with the Department of Electrical and Electronic Engineering, Faculty of Engineering, University of Stellenbosch, Stellenbosch 7600, South Africa (e-mail: kamper@sun.ac.za).

Color versions of one or more of the figures in this paper are available online at http://ieeexplore.ieee.org.

Digital Object Identifier 10.1109/TIA.2013.2295468

I. Introduction

In the case of electrical machines with large diameters and short axial lengths, such as direct-drive PM wind generators, the end effects have a significant influence on the performance of the machine. In many cases, in the design of nonoverlap winding PM machines, the end-winding inductance component is ignored due to the very short end-winding length. This assumption, however, is shown in this paper to be invalid. The largest influence of the end effects on the parameters and the performance of the nonoverlap winding machine are observed in the per-phase inductance value and the short-circuit performance. Under the short-circuit conditions in PM machines, as discussed in [1], the short-circuit current can be extremely high, and undesired braking torque is produced. It is essential that the correct short-circuit current is known as this can influence the design of the PMs due to demagnetization concerns. Moreover, particularly for directly grid-connected systems, as discussed in [2]–[5], it is important to know the amplitude of the maximum short-circuit current during grid fault conditions. It is furthermore important to know the correct short-circuit torque profile of PM wind generators as this will determine the electromagnetic braking capabilities of the generator, as explained in [6]. An incorrect prediction of the per-phase inductance can also result in the power factor of the generator being significantly different from expected. Furthermore, for PM machine control, it is important that the correct machine parameter values are known. It is also important that the correct machine parameters are used in the design of the inductance–capacitance filter that is typically placed on the generator side for PM machine drives.

Some of the most relevant methods and arguments found in literature for the calculation of the end-winding inductance are discussed in the following. In most cases, the end winding is assumed to be fully encapsulated in air, and the end-coil shape is assumed to be circular or semicircular. Examples are the analytical approximation used in [7] and the analytical approach in [8]. A typical analytical method, as proposed in [9], is to combine the two coil ends to form a circular-shaped or oval-shaped coil in air, of which the inductance can be easily calculated from the formulas in [10]. However, in reality, the shape of concentrated coil end windings is not always circular and is, in many cases, much closer to the stack. From the findings in [9] and [11]–[13], it can be observed that the effects of the lamination stack on the end-winding inductances cannot be ignored. In [12] and [13], the method of images, as will be further explained in this paper, is proposed for the calculation of the end-winding inductance. It is also stated in [11] that care should be taken with regard to the rest of the permeable machine structure, e.g., the machine casing and the mounting plate. The most accurate calculation method for the end-winding inductance is the 3-D finite-element (FE) inductance calculation method, as explained in [14] and [15]. In this calculation of the end-winding inductance, the per-phase 2-D FE inductance is first calculated and subtracted from the per-phase 3-D FE-calculated inductance. However, 3-D FE modeling is difficult, and 3-D FE simulations are time consuming, which does not make this method suitable for use in design optimization iterations and in the quick evaluation of the end-winding inductance. In [16], a 2-D FE calculation method for the end-winding inductance is proposed. With this method, some of the other permeable machine structure components can be also taken into account. Another FE method that is proposed in literature to calculate the end-winding inductance is the simplified 3-D FE method reported in [17]. In this case, only the end-winding region is modeled in the 3-D FE method and a small part of the lamination stack. However, even for this much simpler 3-D FE model, the simulation times will be significantly more than that of 2-D FE simulations. Therefore, there is a lack of simple and accurate calculation methods for end-winding inductance in literature, and little mention is made on the effect that this parameter can have on the machine performance.

In [18], it is mentioned that, in addition to the end-winding inductance, there are other aspects that influence the per-phase inductance and short-circuit performance of the machine. Thus, it is not sufficient to only take into account the end-winding inductance component for the calculation of the machine performance. It is found that, by changing the magnetic saturation levels in the machine, a much better match is obtained between the FE results and the measurements. The changes in magnetic saturation levels can be attributed to the variations in the characteristics of the PMs. It is therefore essential that the effects that are caused by the PM end-flux fringing be investigated. Some mention is made in literature regarding this aspect. It is mentioned that, particularly for large diameter, axially short machines [19], machines with a small air gap [20], and at load values higher than the rated values [21], the PM end effects cannot be ignored any longer. In [22] and [23], the output performance parameters are multiplied by a fringing factor and in [24], by a further magnetic saturation correction factor. These factors are calculated by observing the difference in the 3-D and 2-D FE calculations for a specific range of PM machines. In [19], an analytical approach that uses fictitious PM arrays is used to calculate the 3-D PM field distribution.

In this paper, two different analytical methods for the calculation of the end-winding inductance, of which one is a new proposal, and two FE calculation methods are compared with each other with regard to accuracy. An investigation into the effects of the PM end-flux fringing and whether there is a simple method to obtain an indication on the amount of fringing is also launched. Furthermore, the short-circuit characteristics of nonoverlap winding PM machines are investigated to gain a better understanding of the influence of the end effects on these machines. Five different nonoverlap winding PM machines are evaluated in order to obtain a valid comparison and a better indication of the accuracy of the calculation methods, with practical measurements also shown.

II. PM Machines Investigated

An application of the nonoverlap winding PM machines studied in this paper is for wind turbine generators, as in [5] and [25]–[27]. Table I gives some information on the five different PM machines evaluated, and Fig. 1 shows the sections of the five PM machines under consideration. Machines 1–4 are similar in size and power rating, with different coil dimensions and winding configurations. For a further characterization of the different calculation methods, Machine 5, which is a much larger direct-drive wind turbine generator, is also evaluated. All the machines make use of nonoverlap modular windings. Machines 1 and 2 make use of a single layer (SL) winding

TABLE I
DIMENSIONS AND DESCRIPTION OF THE DIFFERENT PM MACHINE STRUCTURES

Machine	1	2	3	4	5
P_g (kW)	15	0.8	1.1	15	350
T_g (Nm)	1000	850	1000	1000	67 kNm
n_s (r/min)	150	9	10.5	150	50
V_s (V)	230	14 mV	7.7	230	230
I_s (A)	23	1400	30	23	511
r_c (mm)	285.0	277.1	277.4	293.5	1150
Aspect	0.160	0.102	0.102	0.170	0.107
w_t (mm)	22.63	26.97	18.81	21.50	43.77
w_c (mm)	18.00	12.00	17.50	8.500	24.90
h_c (mm)	48.90	47.28	25.90	27.00	73.38
h_g (mm)	2.00	2.00	2.00	2.00	4.00
h_m (mm)	6.00	8.00	8.00	6.32	19.25
NdFeB grade	N48H	N48H	N48H	N48H	N35H
Winding	SL	SL	DL	DL	DL
N_c	400	1	230	180	26
q	8	8	16	16	25
n_a	8	8	8	8	5

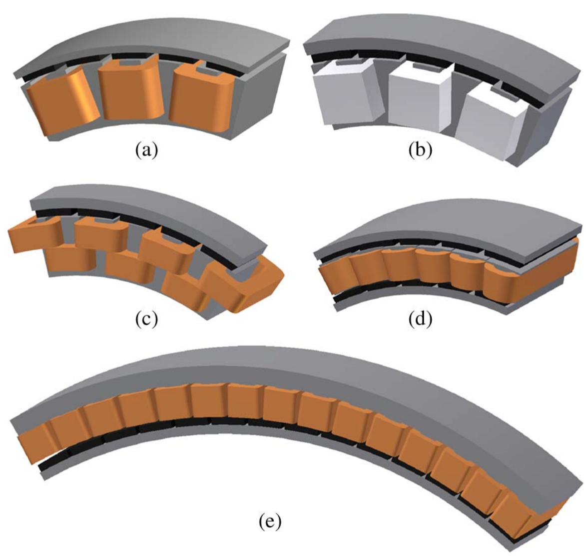

Fig. 1. Sections of the studied PM machines. (a) Machine 1 [25]. (b) Machine 2 [5]. (c) Machine 3 [5]. (d) Machine 4 [26]. (e) Machine 5 [27].

configuration, where every alternate tooth is wound, and Machines 3 to 5 use double layer (DL) windings, where each tooth is wound. Moreover, Machine 2 makes use of a solid bar winding with only one turn. Some of the coil and machine parameters given in Table I and necessary for the calculations are the average coil radius r_c, coil width w_c, the average tooth width w_t, and the height of the coil h_c. The aspect ratio, as commonly used in electrical machine sizing and as given in Table I, is the ratio of axial stack length l to the air-gap diameter D_{ag} of the machine. The rated power and torque of the machines are indicated by P_g and T_g, respectively; the rated speed, by n_s; and the rated root-mean-square voltage and current, by V_s and I_s, respetively. It is clear in Table I and Fig. 1 that several different nonoverlap winding machine topologies are evaluated in this paper, which gives a good indication on the accuracy of the calculation methods considered in this paper.

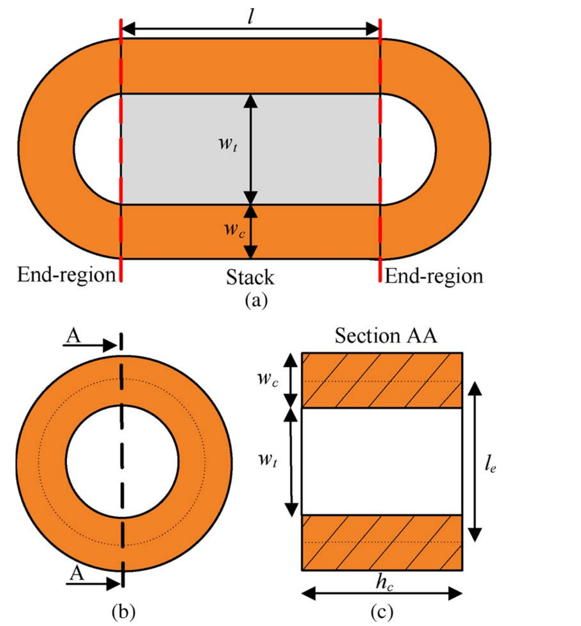

Fig. 2. (a) Top view of the coil. (b) Combination of the two end-coil sections into one circular coil. (c) Cross section of the circular coil.

III. END-WINDING INDUCTANCE CALCULATION

In this section, two analytical calculation methods and the 2-D FE method that is used to calculate the end-winding inductance are explained. The technique that is used to isolate the end-winding inductance from the 3-D FE analysis is also discussed.

A. First Analytical Calculation Method

The first analytical equation presented in this paper makes use of the elementary method of combining the two end-coil sections to form a circular coil in air, as is used in [9]. To calculate the inductance, the formula for a circular air-cored coil with the rectangular cross section given in [10] is used. Fig. 2 shows how the two end-winding sections on both sides of the stack are combined to form the circular coil. For this method, it is assumed that the end-coil sides of all the machines in Table I are circular in shape. From the dimensions of the circular coil, the per-phase end-winding inductance can be expressed from [10] as

$$L_{e(1)} = \frac{1.9739}{n_a^2}\left(\frac{2a^2}{b}\right) N_c^2 qK \quad (\mu\text{H}) \tag{1}$$

where n_a is the number of parallel circuits, N_c is the number of turns per coil, and q is the number of coils per phase. The constant K is given by

$$K = k_1 - k_2 \tag{2}$$

with k_1 and k_2 given in the Appendix as functions of the dimensional variables a, b, and c. These variables are given as $a = 0.5\, l_e$, with the average end length given as $l_e = w_t + w_c$, $b = h_c$, and $c = w_c$.

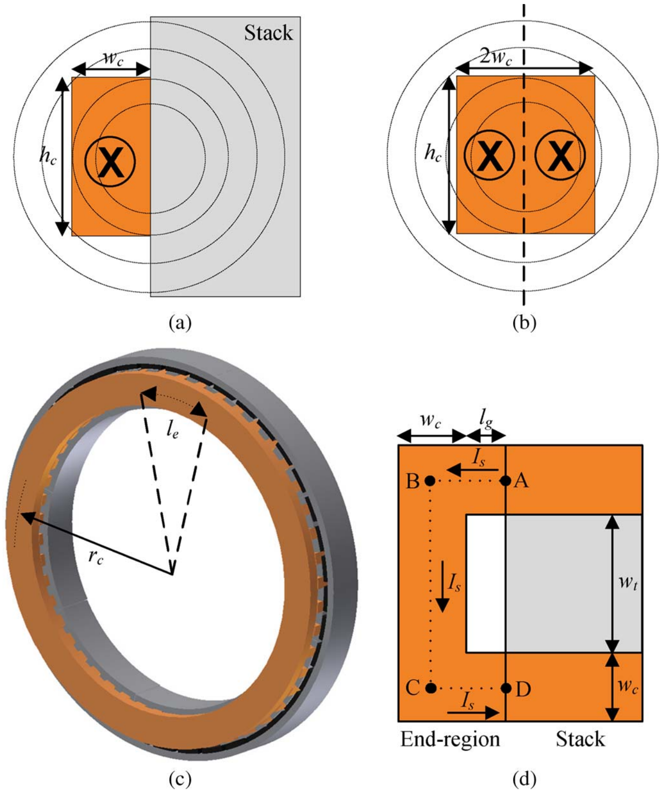

Fig. 3. (a) Cross section of the coil ring with dimensions $h_c \times w_c$ on laminations. (b) Cross section of the coil ring with dimensions $h_c \times 2w_c$ in air. (c) Coil ring with radius r_c used for the second analytical calculation. (d) Actual end-winding path length.

B. Second Analytical Calculation Method

In this approach, the effect of the lamination stack on the end-winding inductance is taken into account using the theory in [12]. In this case, the inductance per end-winding length section is calculated for the large circular coil shown in Fig. 3(c) that has N_c turns and is placed against a laminated core, as shown in the cross-section view in Fig. 3(a). It is experimentally proven in [12] that the laminated core can be taken as a medium of infinite permeability in the calculation of the inductance of the coil at a rated frequency; the idea that the induced eddy currents in the laminations due to the axial end-winding flux prevent the end-winding flux from penetrating the core is found to be untrue in [12]. According to the mirror image principle, the core plane of infinite permeability can be removed and replaced by the mirror image of the circuit, i.e., by using a second coil in air and by placing it as shown in Fig. 3(b). Thus, the circuits in Fig. 3(a) and (b) generate the same amount of flux and have the same flux pattern.

If the two coils in Fig. 3(b) are considered one coil with N_c turns and double the current to generate the same flux, then the inductance of the coil in Fig. 3(a) will be double the inductance of the coil in Fig. 3(b), i.e., $L_{(a)} = 2L_{(b)}$. The inductance $L_{(b)}$ of the coil in air in Fig. 3(b) can be calculated by using (1). To calculate the inductance per end-winding length unit of the large circular coil in Fig. 3(c), the formula in (1) must be multiplied by factor $l_e/2\pi a$, where $2\pi a$, with $a = r_c$, gives the circumference of the large circular coil. Furthermore, to include the inductance of the other half of the end winding, the formula must be further multiplied by a factor 2. Hence, the per-phase end-winding inductance in the second analytical method, with $b = 2w_c$ and $c = h_c$, is calculated by

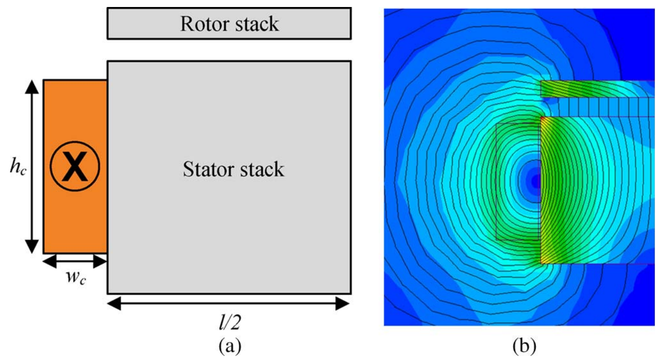

Fig. 4. (a) Model and (b) field plot of the 2-D FE end-winding inductance calculation method.

$$\begin{aligned} L_{e(2)} &= 2 \times \frac{l_e}{2\pi a} \times 2 \left[\frac{1.9739}{n_a^2} \left(\frac{2a^2}{b} \right) N_c^2 qK \right] \\ &= \frac{1.257}{n_a^2} l_e \left(\frac{2a}{b} \right) N_c^2 qK \quad (\mu\mathrm{H}). \end{aligned} \tag{3}$$

At this point, it is very important to specify the correct end-winding length, as will be seen in Section IV-A. In (1) and Fig. 3(c), it is approximated as $l_e = w_t + w_c$. This corresponds to the end-winding section that is indicated by BC in Fig. 3(d). However, observing Fig. 3(d), if Sections AB and CD are taken into account, it is seen that the actual end-winding length is closer to $l_e = w_t + 2w_c + 2l_g$, where l_g is the distance of the end winding from the lamination stack. With the current direction of the end-winding sections AB and CD assumed to be perpendicular to the current flowing in Section BC, it would be normally assumed that these extra end-winding sections are not affected by the lamination stack. From the FE observations, however, it was found that, for this end-winding section, the lamination stack does have an effect. For this particular study, it was found that, for coils with $l_g < 2.5$ mm, the effect of the stack on this section can make a substantial contribution to the overall end-winding result. For coils with $l_g > 2.5$ mm, the observed effect of the lamination stack is not as critical for this particular end-winding section, and it is sufficient to assume that this extra section is solely influenced by air. Thus, a third analytical approach is devised as

$$L_{e(3)} = \begin{cases} L_{e(2)\ (l_e = w_t + 2w_c + 2l_g,\, b = 2w_c)}, & \text{for } l_g < 2.5 \text{ mm} \\ L_{e(1)\ (l_e = w_c + 2l_g,\, b = w_c)} & \\ \quad + L_{e(2)\ (l_e = w_t + w_c,\, b = 2w_c)}, & \text{for } l_g > 2.5 \text{ mm} \end{cases} \tag{4}$$

with $a = r_c$, and $c = h_c$ for all cases.

C. FE Calculation Methods

As no end effects are taken into account by the conventional 2-D FE analysis, a simple 2-D FE method, as proposed in [16], is used to calculate the end-winding inductance. This simplified FE model is shown in Fig. 4 for Machine 1. A conductor with dimensions of $w_c \times h_c$ and model depth l_e is placed next to the half of the rotor and stator stack, as shown in Fig. 4(a).

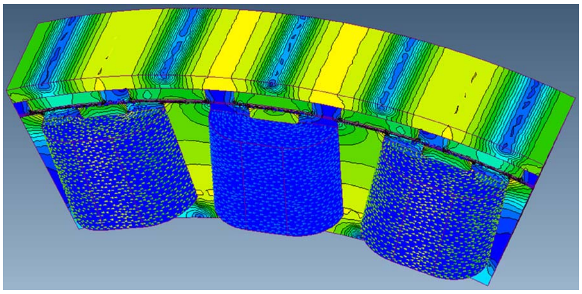

Fig. 5. Three-dimensional FE field plot of Machine 1.

This conductor is defined as a coil and is excited with the rated machine current I_s. From the resulting single static 2-D FE solution, end-winding flux linkage λ_e and the inductance are determined with $L_e = \lambda_e/I_s$.

To shed more light on the accuracy of the analytical methods, the 3-D FE analysis is used to calculate the inductances. Fig. 5 shows the 3-D FE plot of Machine 1. To determine the end-winding inductance of the PM machine, the 2-D total per-phase inductance is subtracted from the 3-D total per-phase inductance. Note that, in this case, the 2-D FE analysis refers to the conventional 2-D FE simulation and not the simplified 2-D FE end-winding inductance calculation method, as in Fig. 4. To eliminate the PM end-winding leakage flux linkage and to simplify the calculation, the PMs are "switched off" in this analysis. This will obviously change the magnetic saturation levels of the core but will have little effect on the end-winding inductance as the reluctance of the end-winding flux path is almost entirely dominated by air.

In both the conventional 2-D and 3-D FE solutions, balanced instantaneous three-phase currents are used to include the mutual flux linkage between the phase windings. The total phase inductance is simply determined from the total phase flux linkage divided by the instantaneous phase current, with $L_s = \lambda_s/I_s$. Thus, in this calculation, one 2-D static FE solution and one 3-D static FE solution are required. This is the most accurate method to calculate the end-winding inductance, as the correct shape of the end-coils and the permeable mediums around the end-coils are taken into account. To investigate the effect of the mutual flux coupling between the phase end windings, the given FE calculations are repeated but with only one phase excited.

IV. Inductance Calculation Results

The explanation of the calculated results in this section is discussed as follows. First, the accuracy of the formulas from literature is evaluated against the results from the FE analysis. Second, the calculation results for all the discussed analytical and FE methods that are applied to the different PM machine topologies are explained.

A. Verification of Formulas

In Table II, the formula (1), which is obtained from the work in [10], for the calculation of the inductance of a circular coil in air is verified. This is done by calculating the inductance values of a 3-D FE model of the end-winding circular coil in

TABLE II
Verification of the Calculation Results in [10] With the 3-D FE Analysis

Machine	Unit	$L_{e(1)}$ [10]	3D-FE	% Error
1	mH	0.340	0.310	8.82
2	nH	2.994	2.823	6.06
3	mH	0.259	0.242	6.56
4	mH	0.135	0.125	7.41
5	μH	21.45	19.94	7.04

TABLE III
Verification of the Method of Images Using the FE Analysis

Coil	Dimensions and turns	Current	Inductance, L (mH)
Fig. 3(a)	$h_c \times w_c$, N_c turns	I_s	1.996
Fig. 3(b)	$h_c \times 2w_c$, N_c turns	$2I_s$	0.994
		$L_{(a)}/L_{(b)}$	**2.008**

TABLE IV
End-Winding Inductance Results Analytically Calculated and Calculated by the FE Analysis

Machine	Unit	$L_{e(1)}$	$L_{e(2)}$	$L_{e(3)}$	2D-FE	3D-FE	L_s
1	mH	0.340	1.814	2.800	1.414	2.904	15.67
2	nH	2.994	10.24	16.80	9.641	17.76	80.16
3	mH	0.259	1.199	1.613	0.962	1.773	7.950
4	mH	0.135	0.681	0.817	0.512	0.922	3.135
5	μH	21.45	108.6	135.2	100.5	155.5	1065

Fig. 2(b) in air of the five PM machines under consideration. An average accuracy of 7.18% is obtained for the five PM machines, which validates the formula in [10]. The method of images, as experimentally analyzed in [12], is also verified again with the FE analysis, as shown in Table III, by calculating the inductances of the conductors defined in Fig. 3(a) and (b). It is clearly found that $L_{(a)} = 2L_{(b)}$, which validates the method of images, as used in this paper.

B. Inductance Calculations

In Table IV, the calculated end-winding inductances of the five PM machines are given using the two analytical and two FE analysis methods. From this, it is clear that the effect of the lamination core cannot be ignored, as the inductance values of the first analytical method are far lower than the values that are obtained from the other methods. The inductance values obtained from the 2-D FE method are also shown to be a bit on the low side. The importance of specifying the correct value for l_e is also clearly seen by comparing the results of $L_{e(2)}$ with $l_e = w_t + w_c$ for all cases and $L_{e(3)}$ with l_e, as defined in (4). It is shown that $L_{e(3)}$, as in (4), gives the best inductance values compared with the values of the 3-D FE method given in Table IV for the five PM machines, particularly for the SL windings. The total per-phase inductance L_s that is calculated using the 3-D FE method is also shown in order to obtain an indication on the relative size of L_e with respect to L_s. It is clear that a large portion of L_s can be attributed to L_e, in some cases, more than 20% of it. To shed some more light on the results of Table IV, Table V gives the mutual phase cross coupling M_c inductance component in percentages for the end-windings of the five machines. It is clearly seen that the DL windings are much more affected by the mutual phase cross coupling, with

TABLE V
EFFECTS OF THE MUTUAL PHASE CROSS COUPLING ON L_e

Machine	Unit	M_c	K_M	$L_{e(3)M_c\neq 0}$	%Error
1	mH	1.73%	1.02	2.856	1.68%
2	nH	1.65%	1.02	17.14	3.58%
3	mH	5.92%	1.11	1.790	0.95%
4	mH	16.8%	1.11	0.907	1.65%
5	μH	10.9%	1.11	150.1	3.60%

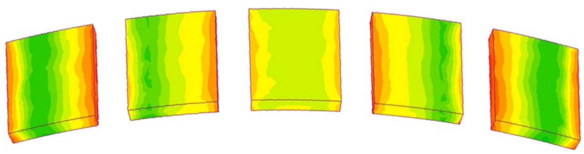

Fig. 6. Flux density plots shown for the PMs of Machine 1 isolated, with the boundary conditions applied to the side of the machine.

a substantial percentage increase in L_e observed. These effects are also less for Machine 3 compared with Machines 4 and 5, which also use a DL winding. The reason is that the two DL coils of Machine 3 are stacked on top of one another, instead of being adjacent, as is the case for Machines 4 and 5.

For a generalized approach to more accurately calculate the end-winding inductance, a mutual phase cross-coupling factor K_M is calculated from the average values of M_c in Table V. To take M_c into account, (4) should be changed to $K_M \times L_{e(3)}$, with $K_M \approx 1.02$ for SL windings, which is almost negligible, and $K_M \approx 1.1$ for DL windings. The new values that are calculated for L_e are shown in Table V. A much better match is obtained between the values of the analytical expression of $K_M \times L_{e(3)}$ and the values from the 3-D FE analysis for the five different nonoverlap winding PM machines. An average error of only 2.3% is observed.

In [18], the effect of the other permeable mediums that are in close proximity to the end windings, particularly the turbine mounting plate, which is typical for PM wind generators on L_e, is also shown. Thus, if it is deemed necessary due to the mechanical topology of the electrical machine, $L_{e(3)}$ can be multiplied by another generalized factor of $K_p \approx 1.1$ to take into account an approximated 10% contribution for the permeable construction mediums.

V. PM END-FLUX FRINGING ESTIMATION

To obtain an indication of the influence of the PM end flux on the machine performance, the 3-D FE analysis is again utilized. The goal is to obtain an expression or a factor to implement in the 2-D FE modeling that matches the 3-D FE and measured results. The prototype generator, as shown in Fig. 1(a), and the 3-D FE field plot in Fig. 5 are used as a case study. Fig. 6 shows the flux density field plot of Machine 1 with the PMs isolated and where a flux tangential boundary condition is applied to the side of the machine in the FE modeling. In the field plot in Fig. 7, the boundary condition is removed, and the simulation is run again. It should be noted that, for the 3-D FE method, half of the machine section is modeled in the axial direction. At the end sections of the PMs, a disturbance can be clearly observed in the flux density plot. This indicates that there are significant fringing effects occurring at the PM ends.

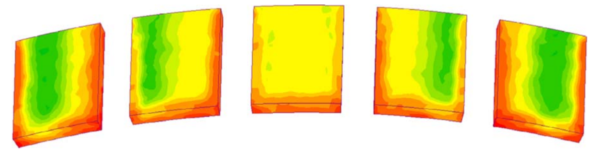

Fig. 7. Flux density plots shown for the PMs of Machine 1 isolated, with no boundary conditions applied to the side of the machine.

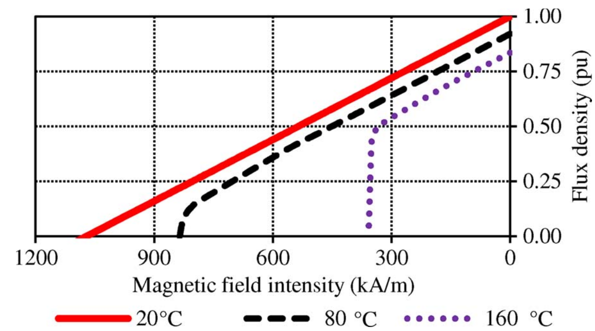

Fig. 8. B–H curves in the second quadrant for the NdFeB N48H PM material for different PM temperatures.

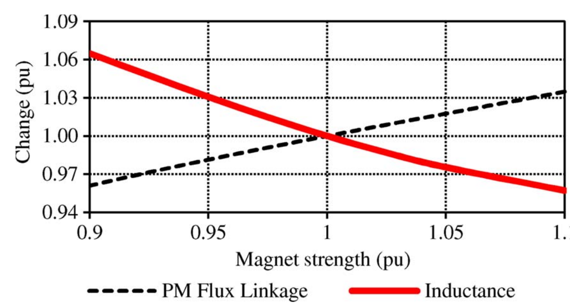

Fig. 9. Per-unit reduction in the FE-calculated per-phase inductance L_s and PM flux linkage λ_m versus the per-unit PM strength for Machine 1.

Furthermore, some of the machine parameters, which include axial length l, magnet height h_m, magnet span σ_m, and air-gap height h_g, were varied, and the flux density plot in Fig. 7 was observed again in each case. The only parameters that are found to influence the flux fringing area that is situated at the end sections of the PMs observably are h_m and h_g. In literature, this disturbance area is used to calculate a constant PM flux fringing factor K_f. The 2-D-calculated PM flux linkage can be then multiplied by this factor with $\lambda'_m = K_f \lambda_m$ to obtain a "corrected" λ'_m. However, due to the large amount of flux fringing around the sides of the PMs, air-gap flux density B_g is reduced, which means that the magnetic saturation levels and the reluctance of the flux paths in the machine change. This means that the reduction in λ_m does not necessarily linearly correspond to K_f.

In this case, rather than using K_f to reduce λ_m or any other 2-D FE machine output performance parameters, the PM strength of the magnets that are used in the 2-D FE modeling is modified by a factor. This is done by modifying the PM B–H curve data used in the FE method by shifting the B–H curve line downward, which is similar with an increase in temperature, as shown in Fig. 8. Usually, in the analysis of the PM B–H curve, the flux density at zero magnetic field intensity is referred to as remanence flux density B_r; hence, in this case, the PM strength is modified with $B'_r = K_f B_r$. Fig. 9 shows the effect

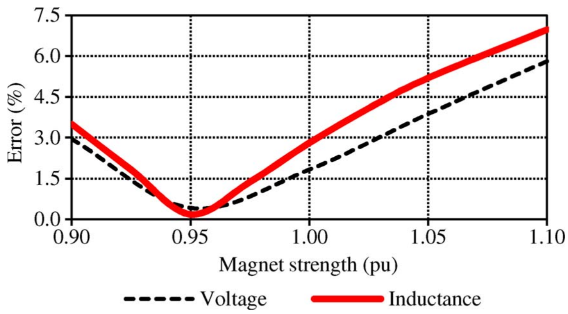

Fig. 10. Percentage error between the measured and FE-calculated phase inductance L_s and voltage V_s versus the per-unit PM strength for Machine 1.

of this variation in the PM strength on λ_m and L_s, again with $L_s = \lambda_s/I_s$, with I_s held constant. One would expect that λ_m would decrease at the same rate as the PM strength, but clearly, λ_m is only changing at less than half of this rate. L_s, on the other hand, increases at about double the rate of change of λ_m for the same reduction in the PM strength. Thus, it is clear that magnetic saturation plays a significant role in the calculation of λ_m and L_s. The proposal in literature to modify the performance parameters that are calculated by the 2-D FE method using a "correction" factor is thus clearly not valid. In order to obtain an indication if the approach to rather modify the PM strength is valid, an experimental analysis is included within the PM end-flux fringing investigation. In Fig. 10, the error between the 2-D FE-calculated and measured open-circuit voltage and the 2-D FE-calculated and measured inductance, with $L_e = L_{e(3)}$, are shown as a function of the magnet strength for Machine 1. The open-circuit voltage is measured at a rated speed of 150 r/min. L_s is calculated using the classical open-circuit and short-circuit tests for synchronous machines [28]. These tests give an adequate indication of L_s, as it is measured at a very low frequency, which means that the core losses can be neglected.

An aspect that should be further considered is the temperature of the PMs, which also causes PM strength variations. Although it is kept constant in the analysis, this aspect should be considered for the PM machines with a high operating temperature or a high PM loss component. Fig. 8 shows the B–H curves in the second quadrant of the NdFeB N48H PM material, as used in this study, at different operating temperatures. The flux density axis is shown (in per units), with the base defined as $B_r = 1.39$ T at 20 °C, with the coercivity point given as $H_c = 1054$ kA/m for the used N48H PM material. Furthermore, inconsistencies in the electrical steel used, as discussed in [29] and [30], can further influence the magnetic saturation levels and flux path reluctances and, thus, λ_m and L_s.

VI. PM Machine Performance Results

Fig. 11 shows the different machines that are being evaluated, with Fig. 11(a) and (b) showing Machine 1 on the test bench and being field tested, respectively. The turbine in Fig. 11(b) has a diameter of 7.2 m, with a rated torque of 1000 $\mathrm{N \cdot m}$ at 150 r/min. The rated wind speed v_w is 11 m/s at a hub height of 16 m. The solid aluminum bar windings for Machine 2 can be clearly seen in Fig. 11(c). Fig. 11(d) shows the DL windings for Machine 3 stacked on top of one another, instead

Fig. 11. Machine 1 [25] on the (a) test bench and (b) being field tested. (c) Machine 2 [5]. (d) Machine 3 [5]. (e) Machine 4 [26]. (f) Machine 5 [27].

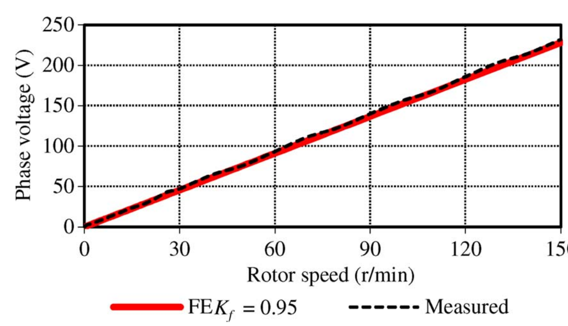

Fig. 12. Measured and FE-calculated open-circuit voltage of Machine 1, with all end effects taken into account, versus the rotor speed.

of adjacent to each other, as is the case for Machines 4 and 5. Machine 4, which is a double-rotor topology, consists of epoxy-casted sections that are then individually placed between the two rotors, as shown in Fig. 11(e). As aforementioned, Machine 5 is a much larger direct-drive wind generator, as shown in Fig. 11(f).

The aim of the measurements shown in this section is to show the effects of L_e, and K_f, which give an indication of the PM flux fringing effect, on the short-circuit characteristics of the machines. Figs. 12 and 13 show the open-circuit voltage and short-circuit current profiles, respectively, of Machine 1 versus the rotor speed with a nominal speed of 150 r/min. The torque versus the speed is shown in Fig. 14 due to the importance of electromagnetic braking in PM wind generators. The torque-versus-speed curves for $v_w = 12$ and 12.5 m/s are for the turbine that is shown in Fig. 11(b). The maximum

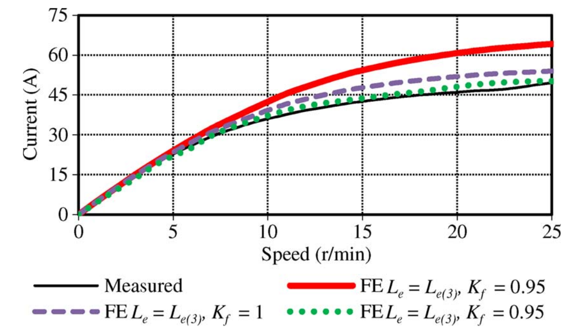

Fig. 13. Measured and FE-predicted steady-state short-circuit current ($I_{\text{rated}} = 23$ A) profiles of Machine 1, with the end effects ignored and taken into account, versus the rotor speed.

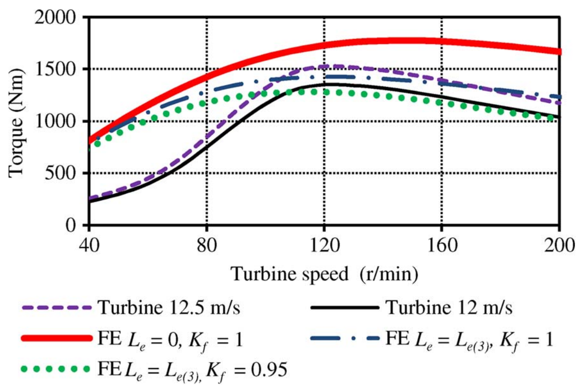

Fig. 14. Turbine torque profiles and steady-state electromagnetic braking torque of Machine 1 ($T_{\text{rated}} = 1000$ N $\cdot$ m), with the end effects ignored and taken into account, versus the turbine speed.

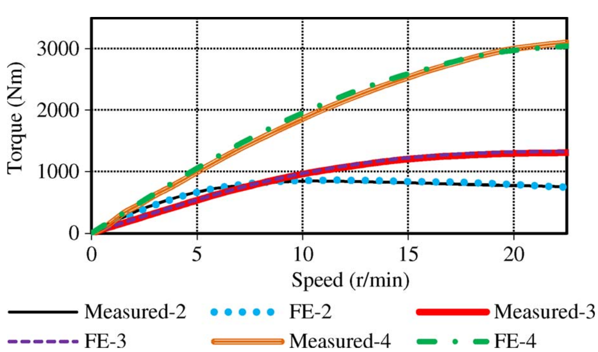

Fig. 15. Measured and FE-predicted steady-state short-circuit torque profiles of Machines 2, 3, and 4, with all end effects taken into account, versus the rotor speed.

braking torque, as defined in [6], is equivalent to $T_b \propto \lambda_m^2/L_s$, and the initial gradient of the torque curve at a low speed is mostly dominated by the per-phase machine resistance. The effect of ignoring L_e and K_f can be clearly seen, particularly if the regions above the rated torque and current are observed with the rated values for the different machines, as given in Table I. By reducing the magnet strength, as in Fig. 10, by a factor of $K_f = 0.95$, a much closer match is obtained between the measured and FE-calculated results. Fig. 15 shows the measured and FE-calculated short-circuit torque profiles with the end-winding inductance and the PM fringing effects taken into account for Machines 1–4, with $K_f = 0.94$ for Machines 2 and 3, and $K_f = 0.95$ for Machine 4. In all cases, a perfect match between the FE calculations and the measurements are obtained.

VII. Conclusion

It has been clearly shown in this paper that the end effects of nonoverlap winding PM machines cannot be ignored in the analysis, particularly in the aforementioned rated region. This is particularly true for the PM machines with low aspect ratios. It is furthermore shown that the commonly used methods that ignore the effect of the laminated core in the calculation of the end-winding inductance are not valid. In this paper, a new analytical approach, with $L_e = L_{e(3)}$ and $M_c \neq 0$, to calculate the end-winding inductance of nonoverlap winding PM machines has been presented. This calculation formula is shown to give consistently good results compared with the 3-D FE analysis for a series of nonoverlap winding PM wind generators. Furthermore, it is also found that the fringing flux occurring at the PM end sections has a substantial effect on the short-circuit characteristics of the machine. It is shown that it is not valid to simply multiply the output performance parameters of the machine by a constant fringing factor, as proposed in literature. A method has been proposed in this paper, in which the PM fringing flux effect is taken into account in the 2-D FE analysis by reducing the PM strength by a certain factor. By means of the 3-D FE method, it was found that, for the investigated machines, a PM strength reduction of about 5% is sufficient to take into account the fringing effect. With the newly proposed end-effect calculation methods, a much better match is obtained between the 2-D FE and practical measurements.

Appendix

Discussed in the following are the procedures to obtain values k_1 and k_2, which are to be used in conjunction with (1), (3), and (4).

A. Calculation of Parameter k_1

For the calculation of k_1, the following series formula, as given in [10], can be used with

$$\begin{aligned} k_1 = & \frac{2\beta}{\pi}\left[\left(\log_e \frac{4}{\beta} - \frac{1}{2}\right) + \frac{\beta^2}{8}\left(\log_e \frac{4}{\beta} + \frac{1}{8}\right)\right] \\ & - \frac{2\beta}{\pi}\left[\frac{\beta^2}{64}\left(\log_e \frac{4}{\beta} - \frac{2}{3}\right) + \frac{5\beta^6}{1024}\right. \\ & \left. \times \left(\log_e \frac{4}{\beta} - \frac{109}{120} - \right) \cdots \right] \end{aligned} \tag{5}$$

where $\beta = b/2a$, with a and b as used in (1), (3), and (4). It is stated in [10] that, for values of β as large as 1/4, the first three terms in (5) will yield an accuracy of 0.001.

B. Calculation of Parameter k_2

The value of k_2 can be found in the lookup tables given in [10] and [18], as a function of c/b and $c/2a$, or as a function of b/c and $c/2a$, with a, b, and c as used in (1), (3), and (4). However, in this paper, to more easily calculate the values of k_2, a curve fitting approximation is made with the help of the MATLAB package for the two tables under consideration. If $b/c \leq 1$, then the following expression, with $x = b/c$ and $y =$

$c/2a$, can be used as

$$k_2 = f_1 e^{f_2 y} + f_3 e^{f_4 y} \tag{6}$$

where

$$\begin{aligned} f_1 &= -0.0638x^2 + 0.3298x - 0.001973 \\ f_2 &= -0.1165x^2 + 0.03898x - 0.3941 \\ f_3 &= 0.06118x^2 - 0.03218x + 0.001861 \\ f_4 &= -1.167x^2 + 0.3721x - 5.587. \end{aligned}$$

If $c/b \leq 1$, then the following expression can be used, with $x = c/b$ and $y = c/2a$, as

$$k_2 = f_1 e^{f_2 y} + f_3 e^{f_4 y} \tag{7}$$

where

$$\begin{aligned} f_1 &= -0.2652x^2 + 0.6943x - 0.01944 \\ f_2 &= -8.246e^{-20.14x} - 0.2779e^{-0.3369x} \\ f_3 &= \frac{-0.001548x + 0.0003029}{x^4 - 2.211x^3 + 1.1485x^2 - 0.2759x + 0.01816} \\ f_4 &= \frac{-2.493x^2 + 0.8325x - 0.4384}{x^3 + 0.03686x^2 - 0.2928x + 0.05966}. \end{aligned}$$

REFERENCES

[1] S. A. Hossain and E. R. Oliveira, "Braking torque analysis of PMSM motor under stator winding failures," in *Proc. Int. Conf. Elect. Mach.*, Marseille, France, 2012, pp. 1597–1601.

[2] B. Hagenkort, T. Hartkopf, A. Binder, and S. Jöckel, "Modelling a direct drive permanent magnet induction machine," in *Proc. ICEM*, Espoo, Finland, 2000, pp. 1495–1499.

[3] H. Müller, M. Pöller, A. Basteck, M. Tilshcher, and J. Pfister, "Grid compatibility of variable speed wind turbines with directly coupled synchronous generator and hydro-dynamically controlled gearbox," in *Proc. 6th Int. Workshop Largescale Integr. Wind Power Transmiss. Netw. Offshore Wind Farms*, Delft, The Netherlands, 2006, pp. 307–315.

[4] S. Grabic, N. Celanovic, and V. A. Katic, "Permanent magnet synchronous generator cascade for wind turbine application," *IEEE Trans. Power Electron.*, vol. 23, no. 3, pp. 1136–1142, May 2008.

[5] J. H. J. Potgieter and M. J. Kamper, "Design of new concept gearless direct-grid connected slip-synchronous permanent magnet wind generator," *IEEE Trans. Ind. Appl.*, vol. 48, no. 3, pp. 913–922, May/Jun. 2012.

[6] J. H. J. Potgieter and M. J. Kamper, "Design considerations in the implementation of an electromagnetic brake for a 15 kW PM wind generator," in *Proc. SAUPEC*, Potchefstroom, South Africa, 2013, pp. 98–103.

[7] M. F. Hsieh, Y. C. Hsu, D. G. Dorell, and K. H. Hu, "Investigation on end winding inductance in motor stator windings," *IEEE Trans. Magn.*, vol. 43, no. 6, pp. 2513–2515, Jun. 2007.

[8] A. M. El-Refaie, Z. Q. Zhu, T. M. Jahns, and D. Howe, "Winding inductances of fractional slot surface-mounted permanent magnet brushless machines," in *Proc. IEEE IAS Annu. Meet.*, Edmonton, AB, Canada, 2008, pp. 1–8.

[9] T. Cox, F. Eastham, and J. Proverbs, "End turn leakage reactance of concentrated modular winding stators," *IEEE Trans. Magn.*, vol. 44, no. 11, pp. 4057–4061, Nov. 2008.

[10] F. W. Grover, *Inductance Calculations: Working Formulas and Tables,* 1st ed. New York, NY, USA: Dover, 1946.

[11] P. J. Lawrenson, "Calculation of machine end-winding inductances with special reference to turbogenerators," *Proc. Inst. Elect. Eng.*, vol. 117, no. 6, pp. 1129–1134, Jun. 1970.

[12] M. J. Kamper and F. S. van der Merwe, "Influence of laminations on axially directed flux in induction motors," in *Proc. ICEM*, Pisa, Italy, 1988, pp. 413–416.

[13] D. Žarko, D. Ban, and R. Klari, "Finite element approach to calculation of parameters of an interior permanent magnet motor," *Automatika*, vol. 46, no. 3/4, pp. 113–122, 2005.

[14] A. Tounzi, T. Henneron, Y. Le Menach, R. Askour, E. Dumetz, and F. Piriou, "3-D Approaches to determine the end winding inductances of a permanent magnet linear synchronous motor," *IEEE Trans. Magn.*, vol. 40, no. 2, pp. 758–761, Mar. 2004.

[15] R. Lin and A. Arkkio, "Calculation and analysis of stator end-winding leakage inductance of an induction machine," *IEEE Trans. Magn.*, vol. 45, no. 4, pp. 2009–2014, Apr. 2009.

[16] R. De Weerdt and R. Belmans, "Squirrel cage induction motor end effects using 2-D and 3-D finite elements," in *Proc. 7th Int. Conf. Elect. Mach. Drives*, Durham, NC, USA, 1995, pp. 62–66.

[17] B. Funieru and A. Binder, "Simulation of electrical machines end effects with reduced length 3D FEM models," in *Proc. Int. Conf. Elect. Mach.*, Marseille, France, 2012, pp. 1430–1436.

[18] J. H. J. Potgieter and M. J. Kamper, "Evaluation of calculation methods and the effects of end-winding inductances on the performance of non-overlap winding PM machines," in *Proc. Int. Conf. Elect. Mach.*, Marseille, France, 2012, pp. 243–249.

[19] Q. Gu and Q. Hao, "Three-dimensional analytic model for permanent magnet electric machines with finite core length," *Elect. Eng.*, vol. 87, no. 6, pp. 305–314, Oct. 2005.

[20] J. Wang, D. Howe, and G. W. Jewell, "Fringing in tubular permanent-magnet machines: Part I. Magnetic field distribution, flux linkage, and thrust force," *IEEE Trans. Magn.*, vol. 39, no. 6, pp. 3507–3516, Nov. 2003.

[21] H. Polinder, J. G. Slootweg, M. J. Hoeijmakers, and J. C. Compter, "Modeling of a linear PM machine including magnetic saturation and end effects: Maximum force-to-current ratio," *IEEE Trans. Ind. Appl.*, vol. 39, no. 6, pp. 1681–1688, Nov./Dec. 2003.

[22] W. Hua, M. Cheng, X. Zhu, and J. Zhang, "Investigation of end-effects in brushless machines having magnets in the stator with doubly salient structure," in *Proc. IEEE INTERMAG Conf.*, San Diego, CA, USA, 2006, p. 197.

[23] T. F. Chan and L. L. Lai, "An axial-flux permanent-magnet synchronous generator for a direct-coupled wind-turbine system," *IEEE Trans. Energy Convers.*, vol. 22, no. 1, pp. 86–94, Mar. 2007.

[24] H. VuXuan, D. Lahaye, H. Polinder, and J. A. Ferreira, "Improved model for design of permanent magnet machines with concentrated windings," in *Proc. IEEE IEMDC*, Niagara Falls, ON, Canada, 2011, pp. 948–954.

[25] J. H. J. Potgieter and M. J. Kamper, "Torque and voltage quality in design optimisation of low cost non-overlap single layer winding permanent magnet wind generator," *IEEE Trans. Ind. Electron.*, vol. 59, no. 5, pp. 2147–2156, May 2012.

[26] J. H. van Wijk and M. J. Kamper, "Double-sided rotor technology for iron-cored permanent magnet wind generators: An evaluation," in *Proc. IEEE ICIT*, Cape Town, South Africa, 2013, pp. 1892–1897.

[27] M. J. Kamper, "Development and test results of South Africa's first 300 kW permanent magnet direct drive grid connected wind generator system," presented at the 18th SAUPEC, Stellenbosch, South Africa, 2009.

[28] S. D. Umans, *Fitzgerald and Kingsley's Electric Machinery,* 7th ed. New York, NY, USA: McGraw-Hill, 2014.

[29] S. Sprague, "An examination of magnetic property variation of specification-acceptable electrical steel," in *Proc. ICEM*, Marseille, France, 2012, pp. 1172–1177.

[30] Z. Cheng, N. Takahashi, B. Forghani, Y. Du, Y. Fan, and H. Wang, "Effect of variation of B-H properties on loss and flux inside silicon steel lamination," *IEEE Trans. Magn.*, vol. 47, no. 5, pp. 1346–1349, May 2011.

Johannes H. J. Potgieter (S'10) received the B.Eng. degree in electrical and electronic engineering and the M.Sc. (Eng.) and Ph.D. (Eng.) degrees in electrical engineering from the University of Stellenbosch, Stellenbosch, South Africa, in 2008, 2011, and 2014, respectively.

He is currently a Postdoctoral Research Assistant with the University of Oxford, Oxford, U.K. His research interests include wind power generation technologies, automotive drive train solutions, and the design and optimization of permanent-magnet and switched reluctance electrical machines.

Maarten J. Kamper (SM'08) received the M.Sc. (Eng.) and Ph.D. (Eng.) degrees from the University of Stellenbosch, Stellenbosch, South Africa, in 1987 and 1996, respectively.

Since 1989, he has been with the Department of Electrical and Electronic Engineering, Faculty of Engineering, University of Stellenbosch, where he is currently a Professor of electrical machines and drives. His research interests include computer-aided design and control of reluctance and permanent-magnet and induction-machine drives.

Dr. Kamper is a Scientist supported by the South African National Research Foundation and a Registered Professional Engineer in South Africa.